

Alternating Stacked Graphene-Conducting Polymer Compact Films with Ultrahigh Areal and Volumetric Capacitances for High-Energy Micro-Supercapacitors

Zhong-Shuai Wu, Khaled Parvez, Shuang Li, Sheng Yang, Zhaoyang Liu, Shaohua Liu, Xinliang Feng,* and Klaus Müllen*

Miniaturized energy storage devices are essential microscale power sources that are small enough to be directly integrated into miniaturized portable, wearable, and implantable electronics.^[1,2] Current commercially available lithium thin-film (LTF) batteries that can be coupled with microelectronics as micropower sources suffer from limited cycle times, low power densities, rapid failures, and lithium-related safety issues.^[3] Alternatively, micro-supercapacitors (MSCs) are a newly emerging family of micro-electrochemical energy storage devices with intriguing features of high power density, fast charge/discharge rate, and long lifetime. MSCs can potentially be operated as stand-alone power sources or as complementary energy storage units of LTF batteries and electrolytic capacitors to power various microelectronics.^[4–7] Notable progress in the development of new nanostructured materials (e.g., graphene), novel thin-film electrode fabrication methods (e.g., roll-to-roll), and advanced device geometries (e.g., in-plane) for MSCs have been reported with enhanced performance.^[1,2,8–12] However, the energy densities for most reported MSCs still fail to compete with those of LTF batteries ($\leq 10 \text{ mWh cm}^{-3}$) for on-chip portable and self-powered operation.

Regardless of the device architecture and electrolyte selection, the major bottleneck for MSCs is the substantially low volumetric capacitance of the micrometer-thick film electrodes (typically $\geq 2 \mu\text{m}$). In general, areal and volumetric capacitances stand in conflict with each other, varying inversely with increasing film thickness. For example, thinner films, such as activated carbon (AC)^[13] and heteroatom-doped graphene,^[14] with a thickness of $< 2 \mu\text{m}$, commonly offer low areal capacitance, typically $< 1 \text{ mF cm}^{-2}$, but exceptionally high volumetric

capacitances that exceed 100 F cm^{-3} .^[13,14] Conversely, thicker films $\geq 2 \mu\text{m}$ are currently the central focus of the pursuit of high areal capacitance ($\geq 10 \text{ mF cm}^{-2}$) for laser-scribed graphene (LSG),^[7] nanoporous carbon (NPC),^[15] onion-like carbon (OLC),^[5] reduced graphene oxide/carbon nanotubes (rGO/CNT),^[16] and vertically aligned carbon nanotubes (VACNT).^[17] However, most of these thick-film devices exhibit low volumetric capacitance ($< 30 \text{ F cm}^{-3}$ for LSG,^[7] OLC,^[5] rGO/CNT^[16] and VACNT^[17]).

The morphology and microstructure of thick-film electrodes largely determine the true performance metrics, e.g., areal and volumetric capacitances, of the MSCs.^[4,18] Ideally, processed micrometer-thick films should synergistically combine three key factors. First, the electrode material must be electrochemically active (a pseudocapacitive component), which is crucial to achieving high capacitance.^[19] Second, the film electrode must have a developed nanoporous structure with mixed ionic–electric conductive pathways, which can promote rapid ion diffusion and electron transport.^[20,21] Third, the film must be highly uniform and densely stacked, yet without added polymer binder and conductive additives, for high volumetric capacitance.^[4,22]

Graphene is a promising 2D material platform for constructing high-performance supercapacitors, including MSCs, due to its large theoretical surface area ($2620 \text{ m}^2 \text{ g}^{-1}$), high intrinsic areal capacitance ($21 \mu\text{F cm}^{-2}$ for a single layer), and gravimetric capacitance (550 F g^{-1}).^[20,23,24] In particular, graphene-based MSCs with in-plane interdigital geometry can sufficiently utilize the unique features of graphene, like 2D thinness and high surface area, for energy storage.^[7,8,25] For instance, Ajayan group^[6] reported the scalable production of a new class of graphene-based monolithic MSCs consisting of rGO microelectrodes and graphene oxide (GO) as separators by laser reduction and patterning of GO films. They demonstrated in-plane MSCs with a circular geometry offering an areal capacitance of 0.51 mF cm^{-2} , nearly twice that of the sandwich structure. Later, El-Kady et al.^[7] described a scalable fabrication of graphene MSCs (denoted as LSG-MSCs) by direct laser writing on GO films using a standard LightScribe DVD burner. By this means, more than 100 MSCs could be readily generated on a single disc in 30 min. Notably, these LSG-MSCs demonstrated an areal capacitance of 2.32 mF cm^{-2} and volumetric capacitance of 3.05 F cm^{-3} at a current density of 16.8 mA cm^{-3} , as well as an ultrahigh power density of 200 W cm^{-3} . Recently, our group developed all-solid-state graphene-based in-plane MSCs based on methane plasma reduction and micropatterning

Dr. Z.-S. Wu, Dr. K. Parvez, S. Yang, Z. Y. Liu,
Prof. K. Müllen
Max-Planck-Institut für Polymerforschung
Ackermannweg 10, 55128 Mainz, Germany
E-mail: muellen@mpip-mainz.mpg.de

S. Li, Dr. S. H. Liu, Prof. X. L. Feng
School of Chemistry and Chemical Engineering
Shanghai Jiao Tong University
200240 Shanghai, P. R. China

Dr. S. H. Liu, Prof. X. L. Feng
Center for Advancing Electronics Dresden (cfaed)
and Department of Chemistry and Food Chemistry
Technische Universität Dresden
01062 Dresden, Germany
E-mail: xinliang.feng@tu-dresden.de

DOI: 10.1002/adma.201501643



of GO films on both rigid and flexible substrates. The fabricated devices exhibited an areal capacitance of $80.7 \mu\text{F cm}^{-2}$, volumetric capacitance of 17.9 F cm^{-3} , ultrahigh scan rate of 1000 V s^{-1} , as well as power density of 495 W cm^{-3} , and energy density of 2.5 mWh cm^{-3} .^[8] However, the reported areal capacitance (from $80.7 \mu\text{F cm}^{-2}$ to 2.32 mF cm^{-2}) and volumetric capacitance (from 3.05 to 17.9 F cm^{-3}) of graphene-based MSCs (with a thickness between 15 nm and $20 \mu\text{m}$) are substantially limited by the electric double-layer capacitive nature of graphene.^[6–8] One promising strategy for MSC development is thus based on micrometer-thick graphene-based hybrid films that include high conductivity together with a binder-free and densely compact structure with both capacitive and pseudocapacitive contributions.^[26]

Herein, we present a universal protocol for the construction of alternating stacked micrometer-thick graphene-conducting polymer compact hybrid films with landmark areal and volumetric capacitances for high-energy MSCs, by taking advantages of the strong coupling and synergistic effect of 2D pseudocapacitive graphene-conducting polymer nanosheets and electrochemically exfoliated graphene (EG). The 2D graphene-based compact films of “PxGy,” where x and y represent the number of deposited graphene-conducting polymer layers (x) and EG layers ($y = x + 1$) are prepared by alternating deposition of the layers of EG and sandwich-like mesoporous graphene-conducting polymer nanosheets, e.g., polyaniline-functionalized graphene (PANI-G) nanosheets or polypyrrole-functionalized graphene (PPY-G) nanosheets. The resultant layer-stacked nanohybrid films are highly conductive (2120 S m^{-1}), uniform, and nanoporous, yet densely packed (1.67 g cm^{-3}). Notably, they can simultaneously deliver an ultrahigh areal capacitance of 368 mF cm^{-2} and a landmark volumetric capacitance of 736 F cm^{-3} at 10 mV s^{-1} for MSCs fabricated based on P2G3 film on the polyethylene terephthalate (PET) substrate, using 16 nm PANI-G nanosheet in aqueous H_2SO_4 electrolyte (denoted as P2G3-MSCs-D), both of which are the highest values among the reported state-of-the-art MSCs. The all-solid-state MSCs fabricated based on P2G3 film on PET substrate using H_2SO_4 /polyvinyl alcohol (PVA) gel electrolyte (denoted as P2G3-MSCs-C) with 210 mF cm^{-2} and 436 F cm^{-3} at 10 mV s^{-1} exhibit remarkable mechanical flexibility without any performance deterioration under bending. Furthermore, the tandem integrated MSCs can efficiently power high-voltage light-emitting diodes. Remarkably, the volumetric energy density of 46 mWh cm^{-3} (10 mV s^{-1}) achieved with compact MSCs based on P2G3 film in ionic liquid electrolyte (1-ethyl-3-methylimidazolium tetrafluoroborate, EMIMBF₄), denoted as P2G3-MSCs-E, is much higher than those of the state-of-the-art MSCs, and LTF batteries ($\leq 10 \text{ mWh cm}^{-3}$).

The fabrication process of MSCs is schematically illustrated in **Figure 1** (see details in the Supporting Information). The nanohybrid films are prepared by alternating deposition of two different 2D nanosheets, e.g., electrochemically EG nanosheets (Figure S1, Supporting Information) and sandwich-like mesoporous graphene-based conducting polymer nanosheets, e.g., PANI-G nanosheets (Figure 1d and Figures S2–S6, Supporting Information) and PPY-G nanosheets (Figure 1e), in sequence on a filtration membrane.

Specifically, the EG and PANI-G nanosheets were first employed to prepare alternating stacked nanohybrid films. The

sandwich-like mesoporous PANI-G nanosheets were synthesized by in situ polymerization of aniline on a GO (Figure S7, Supporting Information) surface, followed by hydrothermal treatment.^[27] Fourier transform infrared, Raman, and X-ray photoelectron spectroscopies (Figures S3–S5, Supporting Information) confirmed the successful formation of PANI-G nanosheets. Scanning electron microscopy (SEM), transmission electron microscopy, and atomic force microscopy revealed a 2D sheet morphology with PANI nanoparticles ($5\text{--}15 \text{ nm}$) homogeneously decorated on graphene with uniform thickness (46 nm) (Figure 1d and Figure S2, Supporting Information). The high specific surface area ($192 \text{ m}^2 \text{ g}^{-1}$) and narrow mesoporous size distribution (average size of 14 nm) were further disclosed by nitrogen adsorption and desorption measurements (Figure S6, Supporting Information). In parallel, high-quality dispersible EG nanosheets (\leq three layers, Figure S1, Supporting Information) produced by electrochemical exfoliation of graphite in aqueous solution were chosen.^[28,29] EG nanosheets exhibited large lateral size ($10 \mu\text{m}$), low oxygen content ($7.5 \text{ at}\%$), and good solution processability (1 mg mL^{-1} in N,N' -dimethylformamide).

2D nanohybrid films of “Px Gy,” where x and y represent the number of PANI-G layers and EG layers, were fabricated by alternate deposition of each dispersion of EG (5 mL , $\leq 0.1 \text{ mg mL}^{-1}$) and PANI-G (5 mL , 2.4 g mL^{-1}) nanosheets in sequence and subsequently dry-transferred onto arbitrary substrates, e.g., a silicon wafer and PET (Figure S8, Supporting Information). Thus, the nanohybrid films with thicknesses ranging from 2 to $20 \mu\text{m}$ were readily produced by adjusting the number (x/y) of these two alternating deposited layers (Figure 1f–i and Figure S9, Supporting Information). Cross-section SEM images of $9 \mu\text{m}$ P4G5 film reveal good adherence to the underlying Si wafer and a well-ordered layer-by-layer (LBL) stacked structure of nanometer-thick ($10\text{--}20 \text{ nm}$, Figure S10, Supporting Information) EG layers and micrometer-thick ($2\text{--}3 \mu\text{m}$) PANI-G layers (Figure 1h,i). Top-view SEM images show continuous, flat films due to the presence of the top covered EG layers (Figure S9, Supporting Information). In sharp contrast, the prepared pure PANI-G film displayed numerous visible millimeter-sized cracks and holes and was not suitable for transferring onto a targeted silicon substrate (Figure S11, Supporting Information). Notably, the maximum electrical conductivity of a P2G3 film on a Si wafer was 2120 S m^{-1} , three orders of magnitude higher than that of PANI-G films ($< 1 \text{ S m}^{-1}$). Similar results were obtained with all other PxGy hybrid films whose thicknesses were determined by a step profiler. Moreover, the PxGy hybrid film showed densely layer-stacked features with a high mass density of 1.67 g cm^{-3} , which is essential for high areal and volumetric capacitances. For comparison, we also attempted to prepare a hybrid film based on PANI-G and rGO sheets; however, this product had an inhomogeneous structure in both the vacuum-filtrated and transferred films due to poor solution processability of rGO sheets (Figure S12, Supporting Information).^[30]

The well-established lithographical microfabrication technique was then applied to the transferred nanohybrid films to produce patterned microelectrodes and corresponding in-plane interdigital MSCs.^[8,9,14] Briefly, an Au layer micropattern was generated by thermal evaporation on the surface of the

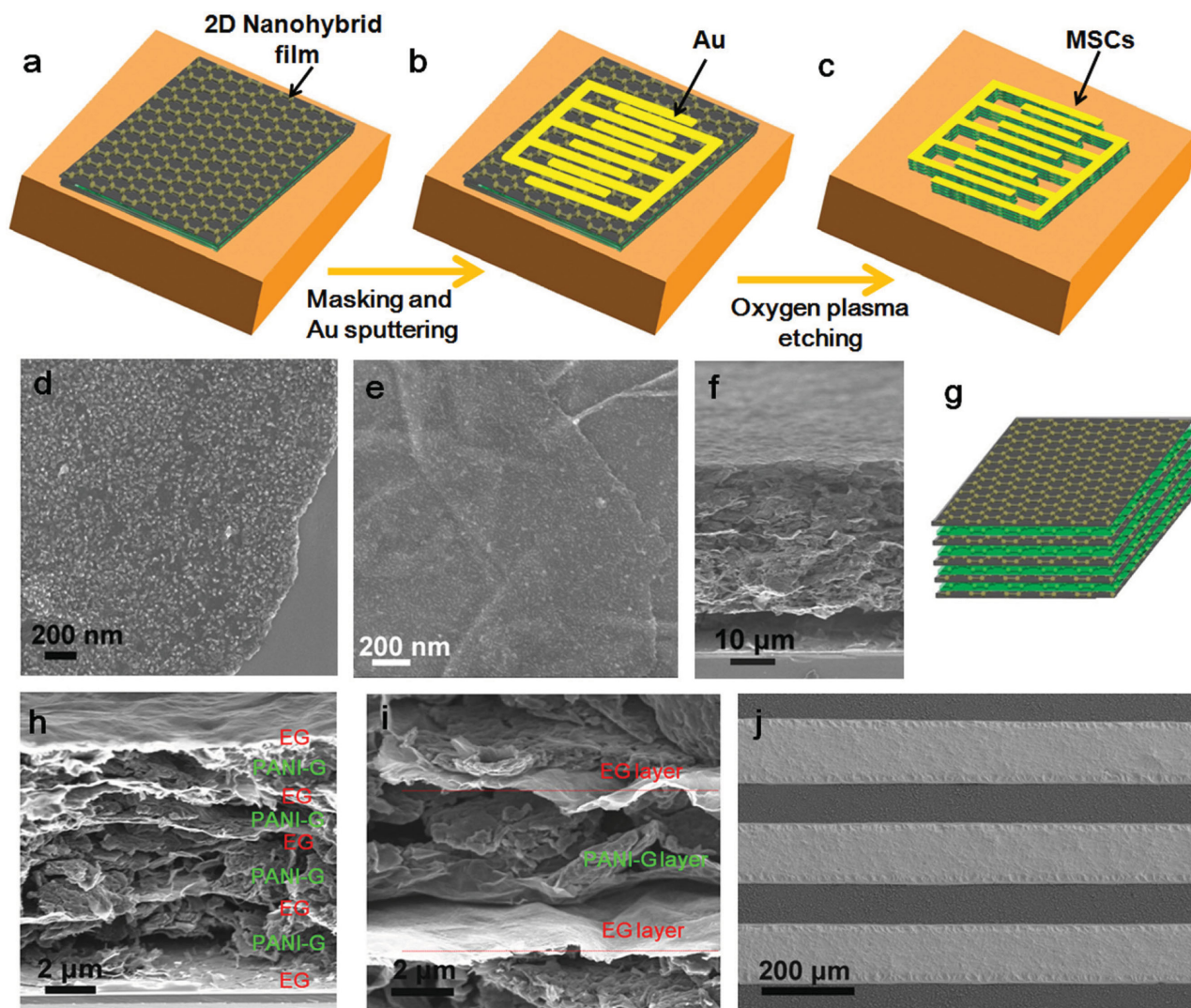


Figure 1. Design and fabrication of alternating stacked graphene-conducting polymer hybrid film for in-plane MSCs. a–c) Illustration of the fabrication procedure for in-plane MSCs with interdigital fingers, including a) transfer of LBL stacked 2D nanohybrid film onto silicon wafer, b) masking micropattern and deposition of gold current collector, c) oxidative etching in oxygen plasma and drop-casting electrolyte. d) SEM image of 46 nm thick PANI-G nanosheet. e) SEM image of PPY-G nanosheet. f) SEM image and g) schematic of micrometer-thick 2D nanohybrid film, showing layer-stacked structure. h,i) Cross-section SEM images of 2D nanohybrid film. j) SEM image with a tilt angle of 30°.

transferred hybrid films with a customized mask (Figure 1a,b). The patterned Au layer acted as a protection mask against oxygen plasma etching to manufacture the designed microelectrodes (Figure 1c). An SEM (Figure 1j) image disclosed well-defined regular widths of $\approx 210 \mu\text{m}$ for fingers and $\approx 70 \mu\text{m}$ for interspaces. EDX elemental mapping analysis and a line scan (Figure S13, Supporting Information) further confirmed the uniform distribution of Au, C, N elements on the interdigital fingers and Si and O elements on the interspaces that are from the top SiO_2 layer on the Si wafer. Finally, the electrolyte, e.g., $\text{H}_2\text{SO}_4/\text{PVA}$, was drop-casted onto the interdigital microelectrodes, and an all-solid-state MSC was thus achieved.

The electrochemical behavior of all-solid-state MSCs based on an alternating stacked 4.5 μm P2G3 film (46 nm thick PANI-G nanosheet) in $\text{H}_2\text{SO}_4/\text{PVA}$ gel electrolyte on Si wafer (denoted as P2G3-MSCs-A) was studied by cyclic voltammetry

(CV) (Figure 2a). To highlight the importance of the alternating stacked structure, we fabricated MSCs based on the films (denoted as M-P2G3) by one-pot filtration of a mixed solution of PANI-G and EG nanosheets with the same content of P2G3. In contrast, the M-P2G3 film exhibited a cracked structural morphology (Figure S14, Supporting Information) and low conductivity of 6 S m^{-1} . We further constructed MSCs based on an EG film ($\approx 110 \text{ nm}$) for comparison (Figure S15, Supporting Information). P2G3-MSCs-A exhibited a pronounced redox response, suggestive of a strong pseudocapacitive effect.^[31] P2G3-MSCs-A presented a greater current density than both M-P2G3-MSCs and EG-MSCs, indicative of higher capacitance from a layer-stacked P2G3 film. In sharp contrast, EG-MSCs displayed classical double-layer capacitive behavior with a lower capacitive response (Figure S15, Supporting Information). The areal and volumetric capacitances of P2G3, M-P2G3,

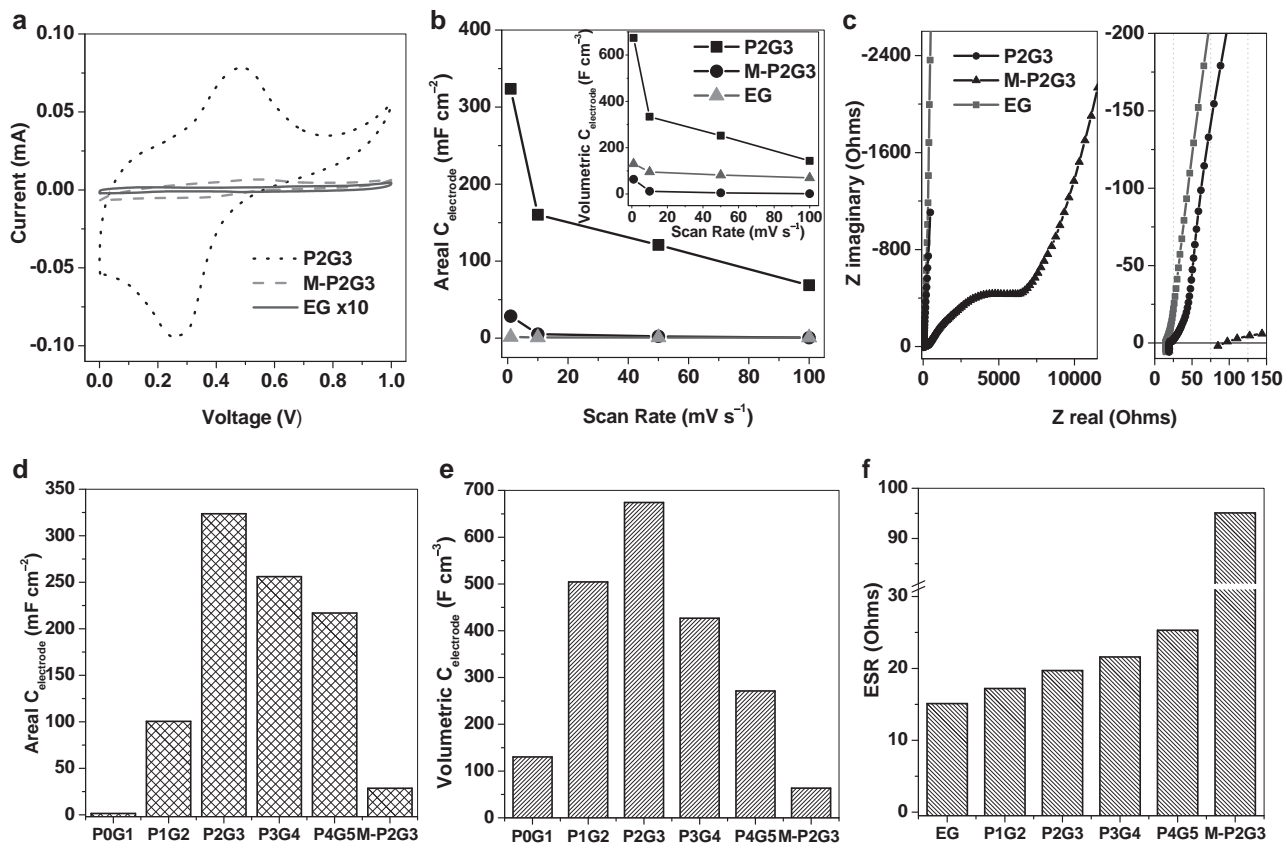


Figure 2. Electrochemical characterizations of P_xG_y films for all-solid-state MSCs on SiO_2/Si wafer. a) CV curves of three MSCs based on P2G3, M-P2G3, and EG films obtained at 1 mV s^{-1} . b) Performance comparison of the areal capacitance and volumetric capacitance (inset) of three films. c) Complex plane plot of three MSCs based on P2G3, M-P2G3, and EG films (left) and the magnified plot of the high-frequency region (right). d) Areal capacitance and e) volumetric capacitance of the layered P_xG_y hybrid films and M-P2G3 film obtained at 1 mV s^{-1} . f) A comparison of ESR values for the P_xG_y hybrid films and M-P2G3 film for all-solid-state MSCs obtained by EIS measurements.

and EG films for MSCs were calculated, as shown in Figure 2b. Remarkably, P2G3-MSCs-A delivered an high areal capacitance of 326 mF cm^{-2} and volumetric capacitance of 675 F cm^{-3} at 1 mV s^{-1} , both of which are superior to those of M-P2G3-MSCs (28.5 mF cm^{-2} and 63.5 F cm^{-3}) and EG-MSCs (1.43 mF cm^{-2} and 130 F cm^{-3}). Furthermore, the resultant P2G3-MSCs-A offered an excellent capacitance even when operated at a high rate; for example, 69 mF cm^{-2} and 143 F cm^{-3} were obtained at 100 mV s^{-1} . On the contrary, the performance of M-P2G3 declined quickly, exhibiting lower capacitances of 1.32 mF cm^{-2} and 0.6 F cm^{-3} at 100 mV s^{-1} .

Electrochemical impedance spectra (EIS) confirmed fast ion transport in P2G3-MSCs-A (Figure 2c and Figure S16, Supporting Information). At low frequency, a large slope with nearly closed 90° was presented in P2G3-MSCs-A, attributable to the highly accessible surface of the layer-stacked film (Figure 2c, left). Furthermore, the equivalent series resistance (ESR) derived from the high-frequency region of P2G3-MSCs-A is only $19.7\ \Omega$, close to that of EG-MSCs ($15.1\ \Omega$) but much lower than that of M-P2G3-MSCs ($95.1\ \Omega$). Remarkably, P2G3-MSCs-A showed quite small charge transport resistance with an invisible semicircle (right plot in Figure 2c), emphasizing the superiority of P2G3 film (high continuity and excellent through-thickness conductivity).

We further investigated areal and volumetric capacitances as a function of film thickness (Figure 2d,e and Figure S17, Supporting Information). Layered hybrid films with varying thicknesses between 2.2 (P1G2) and $4.5\ \mu\text{m}$ (P2G3) offered an increased areal capacitance from 100 to 323 mF cm^{-2} at 1 mV s^{-1} (Figure 2d), which can be explained by the increase of the total accessible electrochemical surface area in the interdigital electrodes. In addition, the volumetric capacitance increases from 504 F cm^{-3} for P1G2 to 675 F cm^{-3} for P2G3 (Figure 2e). As the film thickness increases from 4.5 to $10\ \mu\text{m}$ or more, the capacitance decreases gradually, which can be rationalized by the increase of ESR values from 19.7 to $25.3\ \Omega$ in devices (Figure 2f and Figure S16, Supporting Information). Nevertheless, the thicker films, P3G4 ($6.7\ \mu\text{m}$) and P4G5 ($9.2\ \mu\text{m}$), maintained an areal capacitance of $>210\text{ mF cm}^{-2}$ (Figure 2d) and volumetric capacitance of $>270\text{ F cm}^{-3}$ (Figure 2e). Moreover, the MSCs based on the P2G3 film (using 16 nm thick PANI-G nanosheets, Figure S18, Supporting Information) on silicon wafer using H_2SO_4/PVA gel electrolyte, denoted as P2G3-MSCs-B, had similar capacitive results as the P2G3-MSCs-A based on 46 nm thick PANI-G nanosheets at low scan rate (1 mV s^{-1}), but the former exhibited better rate capability than the latter due to the thinness nature of nanosheets (Figure S19 and Table S1, Supporting Information).

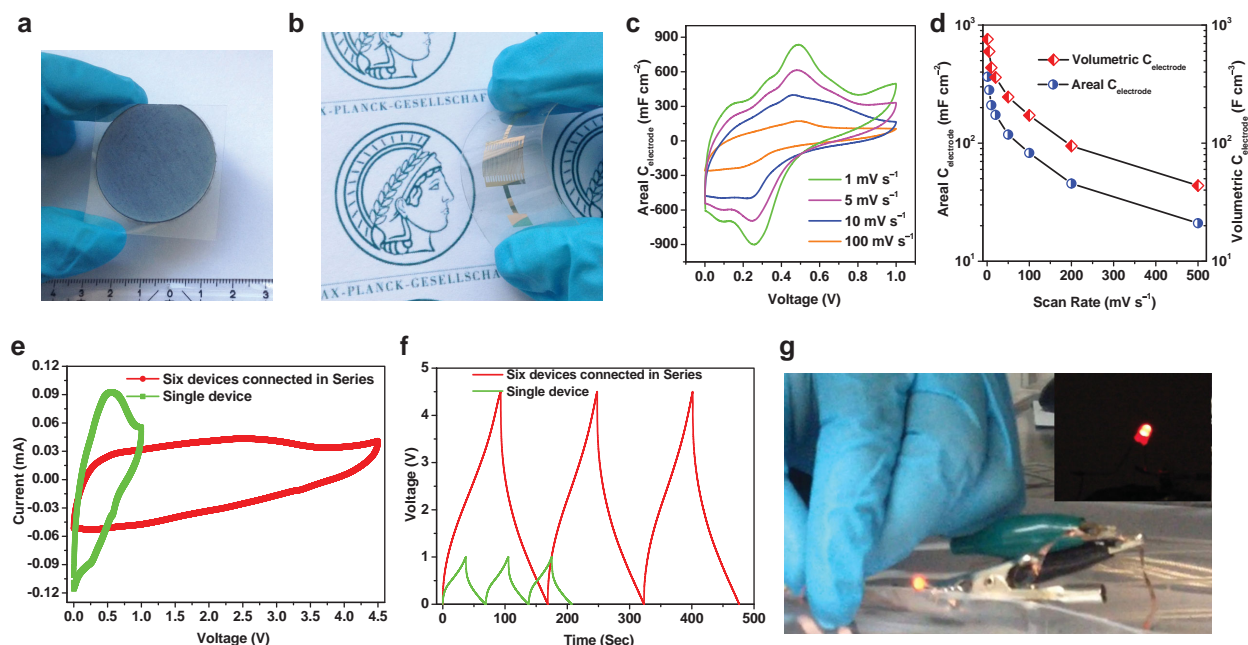


Figure 3. Electrochemical performance of the alternating stacked hybrid films for flexible MSCs. a) Optical image of a transferred $4.5 \mu\text{m}$ thick P2G3 film (16 nm thick PANI-G) with a diameter of 3.6 cm on PET substrate. b) Optical image of a flexible MSC (P2G3-MSCs-C) based on the transferred P2G3 film on PET substrate, exhibiting highly flexible character of the fabricated MSCs. c) CV curves and d) areal and volumetric capacitances of P2G3-MSCs-C. e) CVs obtained at 10 mV s^{-1} and f) galvanostatic charge–discharge curves obtained at 3.3 A m^{-2} of six MSCs connected in series. A single device is shown for comparison. Both of them show the voltage increase from 1 V for single device to 4.5 V for six tandem MSCs in series. g) Optical image of a light-emitting diode (LED) powered by using the four tandem MSCs (charged to 3.0 V). Inset: an LED can be illuminated for more than 30 s by six tandem MSCs (charge to 4.5 V).

The future development of portable and wearable electronics (e.g., roll-up displays and e-paper) often requires light-weight and flexible energy storage devices on chips.^[23] We further adapted our fabrication strategy to construct flexible MSCs on a PET substrate in $\text{H}_2\text{SO}_4/\text{PVA}$ gel electrolyte (P2G3-MSCs-C) and $1 \text{ M H}_2\text{SO}_4$ aqueous electrolyte (P2G3-MSCs-D) (Figure 3 and Figure S20, Supporting Information). For instance, a $4.5 \mu\text{m}$ thick P2G3 film (using 16 nm thick PANI-G) was readily transferred to a PET substrate with high flexibility (Figure S8, Supporting Information). The corresponding devices could be bent or twisted without influencing their structural integrity (Figure 3a,b). Interestingly, the resultant P2G3-MSCs-C exhibited a higher areal capacitance of 210 mF cm^{-2} and volumetric capacitance of 436 F cm^{-3} at 10 mV s^{-1} , as well as better rate capability than those of P2G3-MSCs-B on Si wafers (206 mF cm^{-2} and 428 F cm^{-3} at 10 mV s^{-1}) (Figure 3c,d and Table S1, Supporting Information). We attribute this result to the intimate contact between the electrode and elastic PET substrate, which leads to an increased conductivity of 2450 S m^{-1} . Furthermore, P2G3-MSCs-C showed exceptional electrochemical stability under various bending angles of $0, 30, 60, 90, 150,$ and 180° (Figure 4a). It can be disclosed that CV curves with different bending angles changed slightly (Figure 4b), and 98.2% of initial capacitance was kept for bending even at 180° (Figure 4c), demonstrative of the excellent mechanical flexibility of the P2G3-MSCs-C device. Additionally, P2G3-MSCs exhibited good cycling stability under flat and constant bending state, maintaining $\approx 92.6\%$ of the initial performance after 1000 cycles (Figure 4d and Figure S21a, Supporting

Information), and long-term stability with $\approx 86.6\%$ of capacitance retention after 5000 cycles (Figure S21b,c, Supporting Information).

To demonstrate the superior performance of these MSCs, we compared in-plane MSCs (P2G3-MSCs-D) with classical sandwich supercapacitors using the same P2G3 films (area size of $1 \text{ cm} \times 1 \text{ cm}$) on PET substrates and aqueous H_2SO_4 electrolytes. Remarkably, P2G3-MSCs-D had a landmark areal capacitance of 368 mF cm^{-2} and volumetric capacitance of 736 F cm^{-3} at 10 mV s^{-1} , both of which are higher than those of the sandwich supercapacitors, 343 mF cm^{-2} and 686 F cm^{-3} at 10 mV s^{-1} , respectively (Figure S22, Supporting Information). Note that the obtained areal and volumetric capacitances for P2G3-MSCs-D (368 mF cm^{-2} and 736 F cm^{-3} at 10 mV s^{-1}) are the highest values among the state-of-the-art reported MSCs (the maximum areal capacitance of 40.2 mF cm^{-2} was achieved for NPC^[15] and the volumetric capacitance of 390 F cm^{-3} was achieved for AC^[13]) (Figure S23, Supporting Information). To our knowledge, this is the best performance of MSCs with simultaneously ultrahigh areal and volumetric capacitances reported to date. Further, the resulting aqueous P2G3-MSCs-D exhibited impressive rate capability, for instance, presenting areal capacitance of 229 mF cm^{-2} and volumetric capacitance of 460 F cm^{-3} at scan rate of 50 mV s^{-1} , and 166 mF cm^{-2} and 331 F cm^{-3} at 100 mV s^{-1} . Even at ultrahigh operation scan rate of 5000 mV s^{-1} , P2G3-MSCs-D still presented a significant capacitance of 11.0 mF cm^{-2} and 22.2 F cm^{-3} (Figure S22, Supporting Information). Moreover, the resulting aqueous P2G3-MSCs-D delivered an excellent volumetric capacitance of

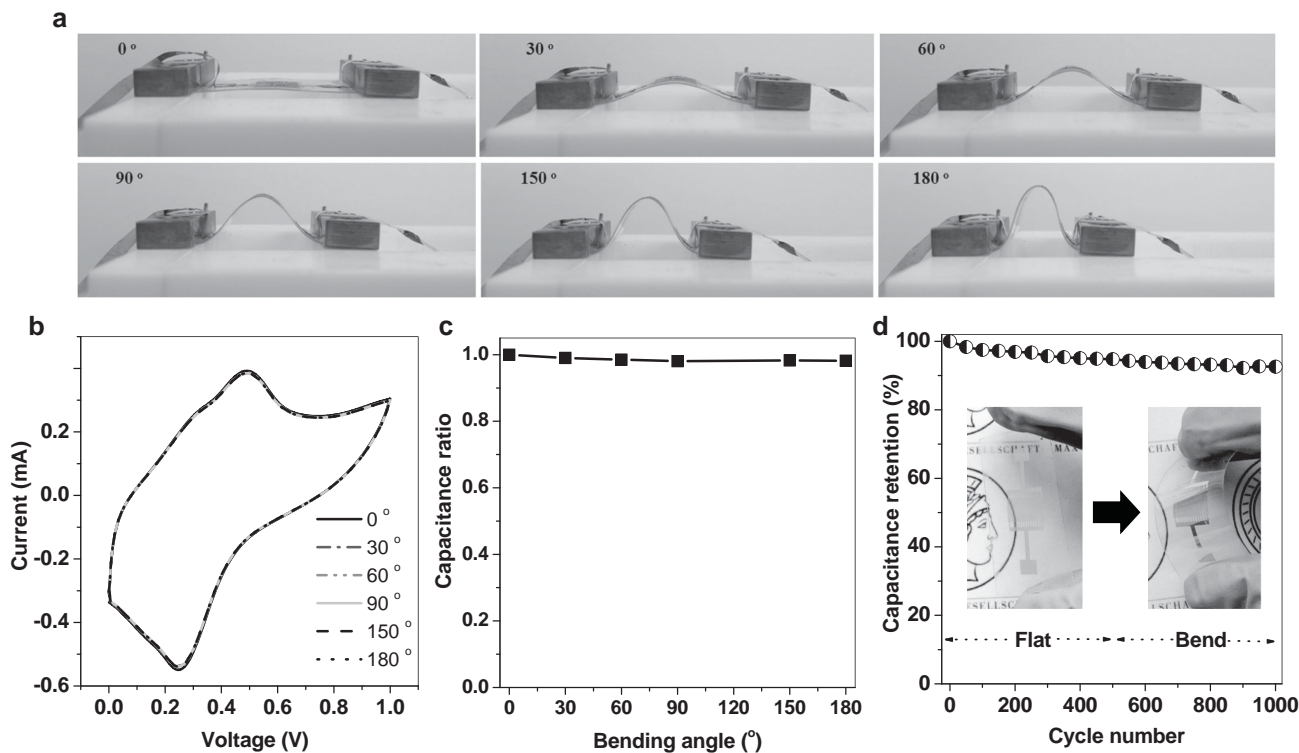


Figure 4. The flexibility and cycling stability of P2G3-MSCs-C on PET substrate. a) Photographs of P2G3-MSCs-C bended with different angles. b) CV curves of P2G3-MSCs-C bended with different angles at 10 mV s^{-1} . c) Evolution of the capacitance ratio as a function of bending angle. d) Cycling stability of P2G3-MSCs-C obtained at 50 mV s^{-1} for 1000 cycles under flat and bending state. Inset shows the optical images of the device in flat and bend states.

142 F cm^{-3} (at 10 mV s^{-1}) based on the whole device, at least 20 times higher than that of the sandwich supercapacitors (only 6.4 F cm^{-3} at 10 mV s^{-1}) (Figure S22, Supporting Information). Even at an ultrahigh scan rate of 5000 mV s^{-1} , a volumetric capacitance of 4.3 F cm^{-3} was retained for aqueous P2G3-MSCs-D. Overall, the superior electrocapacitive behavior of P2G3-MSCs-D can be substantially attributed to the full optimization of the suitable film thickness (e.g., P2G3), thin PANI-G nanosheet (16 nm), elastically flexible PET substrate, and high ionic conductivity of the aqueous electrolyte (see detailed comparison in Table S1 and discussion in Supporting Information).^[32]

To date, there have been a few demonstrations of MSCs as micropower sources for potential applications due to their low energies in a single MSC or MSC pack, even via serial and/or parallel connections. Our patterned nanohybrid film MSCs could be directly integrated in series and/or parallel connections to increase output voltage or total capacitance (Figure 3e–g and Figure S24, Supporting Information). Figure 3e,f shows six integrated all-solid-state MSCs in series, presenting a sufficiently high applied voltage of $\approx 4.5 \text{ V}$, which can essentially power an LED light for tens of seconds (Figure 3g). Further, tandem MSCs connected in a 3 series \times 2 parallel fashion exhibited simultaneous improvement of both voltage and current outputs (Figure S24, Supporting Information). This result highlights the great potential of our MSCs, which can be directly coupled into a circuit to operate numerous micro-devices requiring variable operation voltages.

Energy density is a critical parameter used to compare different types of energy storage systems. In general, a high volumetric energy density in MSCs is an important feature for portable microelectronics.^[2,18] Figure 5 presents Ragone plot related to energy and power densities of our MSCs in different electrolytes compared with reported MSCs and LTF batteries. Note that most reported carbon-based MSCs show low energy densities of $<5 \text{ mWh cm}^{-3}$, e.g., about 2.0 mWh cm^{-3} for LSG,^[7] 2.5 mWh cm^{-3} for MPG,^[8] 3.2 mWh cm^{-3} for CDC,^[22] 4.8 mWh cm^{-3} for PDPC,^[33] 1.9 mWh cm^{-3} for NPG,^[15] IPC (2.3 mWh cm^{-3}),^[34] 1.6 mWh cm^{-3} for OLC,^[5] and 4.0 mWh cm^{-3} for LWG,^[6] which are apparently not comparable to the commercial available LTF batteries ($\approx 10 \text{ mWh cm}^{-3}$) (Figure 5b). Remarkably enough, our MSCs have a maximum energy density of 11.7 mWh cm^{-3} for P2G3-MSCs-C in $\text{H}_2\text{SO}_4/\text{PVA}$ gel electrolyte, 21.1 mWh cm^{-3} for P2G3-MSCs-D in H_2SO_4 aqueous electrolyte, and 46.0 mWh cm^{-3} for P2G3-MSCs-E in ionic liquid electrolyte (EMIMBF₄, Figure 5 and Figure S25, Supporting Information) obtained at 10 mV s^{-1} , which are much higher than those of state-of-the-art carbon-based MSCs, and LTF batteries^[5] (Figure 5b). Furthermore, the P2G3-MSCs-D in aqueous electrolyte possess a significant volumetric power density of $10\,650 \text{ mW cm}^{-3}$ (at 5000 mV s^{-1}) within an extremely short discharging time of 0.2 s (Figure 5a), suggestive of high-power capability of our MSCs.

The landmark performance of the alternating stacked graphene-conducting polymer hybrid films for MSCs is attributed to the unique alternating stacked structure, with a strong coupling effect from the 2D pseudocapacitive PANI-G and

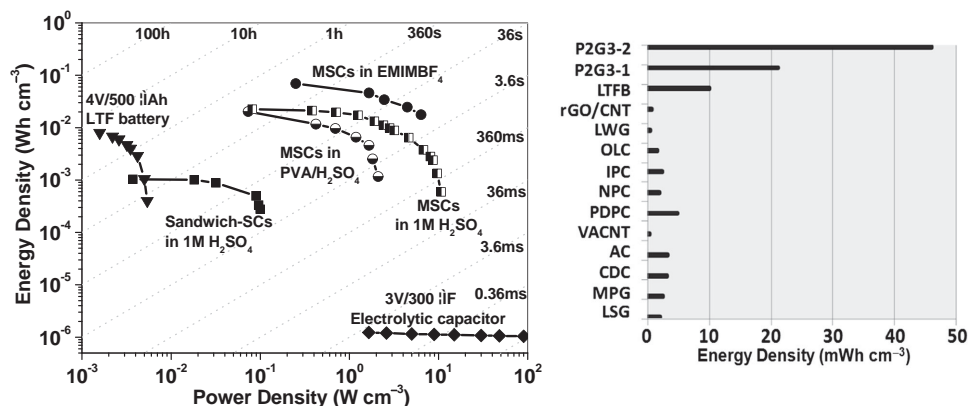


Figure 5. Performance comparison of P2G3-MSCs with various carbon-based MSCs. a) Ragone plot of P2G3-MSCs in different electrolytes, sandwich supercapacitors (sandwich SCs), LTF battery (LTFB, 4 V/500 μ Ah) and electrolytic capacitor (3 V/300 μ F). b) Comparison of energy density of P2G3-MSCs-D and P2G3-MSCs-E with the state-of-the-art carbon-based MSCs. LSG: 7.6 μ m;^[7] MPG: methane plasma-reduced graphene, 15 nm;^[8] CDC: 0.8–1 μ m,^[22] and 2 μ m;^[4] AC: 1.5 μ m;^[13] VACANT: 15 μ m;^[17] PDPC: 1 μ m;^[33] NPC: 5 μ m;^[15] IPC: inkjet-printed carbon, 1–2 μ m;^[34] OLC: 7 μ m;^[5] LWG: laser written graphene oxide film, 20 μ m;^[6] rGO/CNT: 6 μ m;^[16] P2G3-1: P2G3-MSCs-D with 1M H₂SO₄ aqueous electrolyte; P2G3-2: P2G3-MSCs-E with EMIMBF₄ electrolyte. For comparison, the values of energy densities for P2G3-MSCs-D and P2G3-MSCs-E used in (b) were achieved at 10 mV s⁻¹. Note that some values of energy densities are calculated from the given electrode or device capacitance after taking into account of the main parameters, including the widths of the fingers and the interspaces, and the film thickness.

capacitive EG nanosheets. First, the mesoporous graphene-coupled PANI nanosheets with easily accessible ion-transporting channels account for the additional pseudocapacitance and thus the remarkable increase of total capacitance. Second, the flexible EG layer provides an elastic spatial confinement effect to accommodate the adjacent PANI layers, which can (i) promote the formation of continuous films and buffer large volume changes of redox PANI-G sheets during the charge–discharge processes, (ii) serve as a capacitive layer for charge storage, and (iii) provide an electron-conducting pathway for rapid electron transport in the film. Third, the ultrathinness and mechanical flexibility of EG and PANI-G nanosheets by alternate deposition and pressure transfer form a highly compact and binder-free film,^[35] and the in-plane interdigital architecture in MSCs is helpful for utilizing the thinness of 2D nanosheets for charge storage.^[8,9,14]

Apart from using PANI-G nanosheets, our proposed fabrication strategy can be readily extended to other alternating stacked 2D nanohybrid films by incorporating pseudocapacitive components for MSCs. For instance, PPY-G nanosheets (Figure 1e) for constructing such hybrid films for MSCs are demonstrated in Figures S26 and S27 (Supporting Information). The resultant all-solid-state MSCs, with a film thickness of 5 μ m, exhibited an areal capacitance of 196 mF cm⁻², volumetric capacitance of 377 F cm⁻³, and energy density of 10.1 mWh cm⁻³ at 10 mV s⁻¹ (Figure S28, Supporting Information). Therefore, these achieved compact MSCs have great promise as micropower sources for direct integration into various electronic circuits for future portable, wearable, and implantable microelectronics.

Supporting Information

Supporting Information is available from the Wiley Online Library or from the author.

Acknowledgements

This work was financially supported by the ERC Grant on 2DMATER and NANOGRAPH, EU Project GENIUS and MoQuas, DFG SPP 1459, BMBF Insolcell and EC under Graphene Flagship (No. CNECT-ICT-604391). The authors thank G. Glaßer for the kind help with SEM and EDX mapping measurements.

Received: April 7, 2015
Revised: May 7, 2015
Published online: June 3, 2015

- [1] Z. S. Wu, X. L. Feng, H. M. Cheng, *Natl. Sci. Rev.* **2014**, *1*, 277.
- [2] M. Beidaghi, Y. Gogotsi, *Energy Environ. Sci.* **2014**, *7*, 867.
- [3] D. R. Rolison, R. W. Long, J. C. Lytle, A. E. Fischer, C. P. Rhodes, T. M. McEvoy, M. E. Bourga, A. M. Lubers, *Chem. Soc. Rev.* **2009**, *38*, 226.
- [4] J. Chmiola, C. Largeot, P. L. Taberna, P. Simon, Y. Gogotsi, *Science* **2010**, *328*, 480.
- [5] D. Pech, M. Brunet, H. Durou, P. H. Huang, V. Mochalin, Y. Gogotsi, P. L. Taberna, P. Simon, *Nat. Nanotechnol.* **2010**, *5*, 651.
- [6] W. Gao, N. Singh, L. Song, Z. Liu, A. L. M. Reddy, L. J. Ci, R. Vajtai, Q. Zhang, B. Q. Wei, P. M. Ajayan, *Nat. Nanotechnol.* **2011**, *6*, 496.
- [7] M. F. El-Kady, R. B. Kaner, *Nat. Commun.* **2013**, *4*, 1475.
- [8] Z. S. Wu, K. Parvez, X. L. Feng, K. Müllen, *Nat. Commun.* **2013**, *4*, 2487.
- [9] Z. S. Wu, K. Parvez, X. Feng, K. Müllen, *J. Mater. Chem. A* **2014**, *2*, 8288.
- [10] K. Wang, W. J. Zou, B. G. Quan, A. F. Yu, H. P. Wu, P. Jiang, Z. X. Wei, *Adv. Energy Mater.* **2011**, *1*, 1068.
- [11] Z. Q. Niu, L. Zhang, L. L. Liu, B. W. Zhu, H. B. Dong, X. D. Chen, *Adv. Mater.* **2013**, *25*, 4035.
- [12] Y. G. Zhu, Y. Wang, Y. Shi, J. I. Wong, H. Y. Yang, *Nano Energy* **2014**, *3*, 46.
- [13] L. Wei, N. Nitta, G. Yushin, *ACS Nano* **2013**, *7*, 6498.
- [14] Z. S. Wu, K. Parvez, A. Winter, H. Vieker, X. Liu, S. Han, A. Turchanin, X. Feng, K. Müllen, *Adv. Mater.* **2014**, *26*, 4552.

- [15] C. W. Shen, X. H. Wang, W. F. Zhang, F. Y. Kang, *Sci. Rep.* **2013**, *3*, 2294.
- [16] M. Beidaghi, C. L. Wang, *Adv. Funct. Mater.* **2012**, *22*, 4501.
- [17] A. Ghosh, V. T. Le, J. J. Bae, Y. H. Lee, *Sci. Rep.* **2013**, *3*, 2939.
- [18] Y. Gogotsi, P. Simon, *Science* **2011**, *334*, 917.
- [19] X. Y. Lang, A. Hirata, T. Fujita, M. W. Chen, *Nat. Nanotechnol.* **2011**, *6*, 232.
- [20] Y. W. Zhu, S. Murali, M. D. Stoller, K. J. Ganesh, W. W. Cai, P. J. Ferreira, A. Pirkle, R. M. Wallace, K. A. Cychosz, M. Thommes, D. Su, E. A. Stach, R. S. Ruoff, *Science* **2011**, *332*, 1537.
- [21] M. R. Lukatskaya, O. Mashtalir, C. E. Ren, Y. Dall'Agnese, P. Rozier, P. L. Taberna, M. Naguib, P. Simon, M. W. Barsoum, Y. Gogotsi, *Science* **2013**, *341*, 1502.
- [22] M. Heon, S. Lofland, J. Applegate, R. Nolte, E. Cortes, J. D. Hettinger, P. L. Taberna, P. Simon, P. H. Huang, M. Brunet, Y. Gogotsi, *Energy Environ. Sci.* **2011**, *4*, 135.
- [23] M. F. El-Kady, V. Strong, S. Dubin, R. B. Kaner, *Science* **2012**, *335*, 1326.
- [24] X. W. Yang, C. Cheng, Y. F. Wang, L. Qiu, D. Li, *Science* **2013**, *341*, 534.
- [25] J. J. Yoo, K. Balakrishnan, J. S. Huang, V. Meunier, B. G. Sumpter, A. Srivastava, M. Conway, A. L. M. Reddy, J. Yu, R. Vajtai, P. M. Ajayan, *Nano Lett.* **2011**, *11*, 1423.
- [26] C. Liu, F. Li, L. P. Ma, H. M. Cheng, *Adv. Mater.* **2010**, *22*, E28.
- [27] S. Li, D. Wu, C. Cheng, J. Wang, F. Zhang, Y. Su, X. Feng, *Angew. Chem. Int. Ed.* **2013**, *52*, 12105.
- [28] K. Parvez, R. J. Li, S. R. Puniredd, Y. Hernandez, F. Hinkel, S. H. Wang, X. L. Feng, K. Müllen, *ACS Nano* **2013**, *7*, 3598.
- [29] K. Parvez, Z. S. Wu, R. J. Li, X. J. Liu, R. Graf, X. L. Feng, K. Müllen, *J. Am. Chem. Soc.* **2014**, *136*, 6083.
- [30] Z. S. Wu, W. Ren, L. Gao, B. Liu, C. Jiang, H. M. Cheng, *Carbon* **2009**, *47*, 493.
- [31] J. J. Xu, K. Wang, S. Z. Zu, B. H. Han, Z. X. Wei, *ACS Nano* **2010**, *4*, 5019.
- [32] C. Z. Meng, C. H. Liu, L. Z. Chen, C. H. Hu, S. S. Fan, *Nano Lett.* **2010**, *10*, 4025.
- [33] B. Hsia, M. S. Kim, M. Vincent, C. Carraro, R. Maboudian, *Carbon* **2013**, *57*, 395.
- [34] D. Pech, M. Brunet, P. L. Taberna, P. Simon, N. Fabre, F. Mesnilgrete, V. Conedera, H. Durou, *J. Power Sources* **2010**, *195*, 1266.
- [35] C. Wu, X. Lu, L. Peng, K. Xu, X. Peng, J. Huang, G. Yu, Y. Xie, *Nat. Commun.* **2013**, *4*, 2431.